Supporting Information

Cartilage-Inspired Rapid In-Situ Fabrication of Seamless Interlocked Electrolyte-Electrode Interface for High-Performance Flexible Supercapacitors

Yu Guo[a], Yinghui Shang[*a], Bingqian Jiao[a], Yuting Guo[a], Yujing Tang[a], Shen Saiji[a],

Dongbei Wu[a], Xia Wang[a], Wenju Li[*a], Qigang Wang[*b]

[a] Frontiers Science Center for Intelligent Autonomous Systems

School of Chemical Science and Engineering

Tongji University

Shanghai 200092, P. R. China

[b] Translational Research Institute of Brain and Brain-Like Intelligence Shanghai
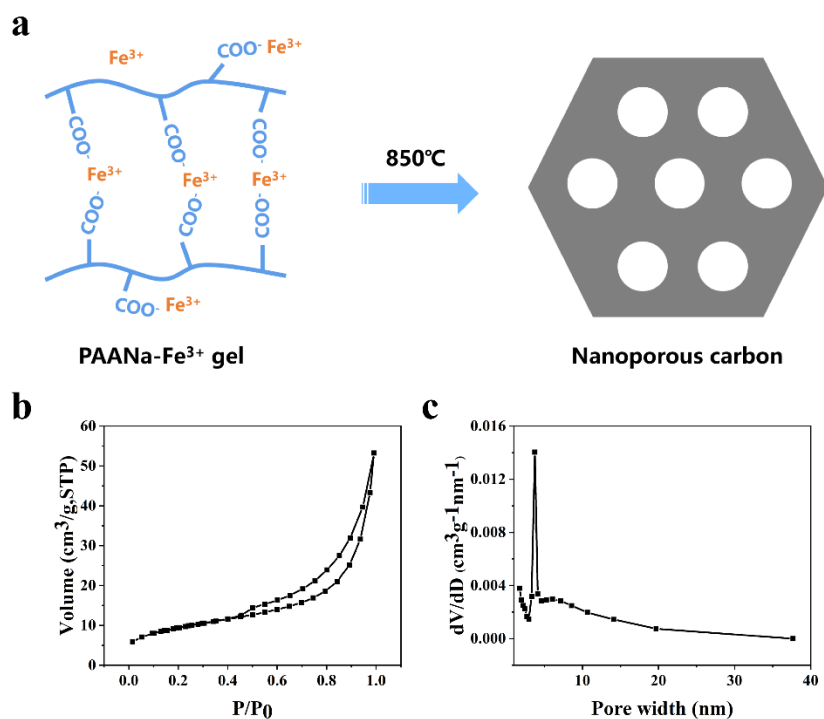
Fourth People's Hospital

School of Medicine

Tongji University

Shanghai 200434, P. R. China

*Corresponding author. E-mail: wangqg66@tongji.edu.cn (Qigang wang);

1234045@tongji.edu.cn (Yinghui Shang); wjli@tongji.edu.cn (Wenjun Li)

S1 Supplementary Figures

Fig. S1. The Schematic diagram of preparation of nanoporous carbon material and BET characterization. (a) PAANa/FeCl$_3$ composites were firstly mixed under 2:1 mass ratio and then added into distilled water to obtain homogeneous polymer matrix, followed by carbonization under 850℃ for 3h. (b) Nitrogen absorption/desorption isotherms of NC obtained at 77 K. (c) Based on the Barrett-Joyner-Halenda method for pore size analysis. BET surface area, total pore volume and average pore size is 33.6160 m^2/g, 0.0807 cm^3/g, and 9.6026 nm, respectively.
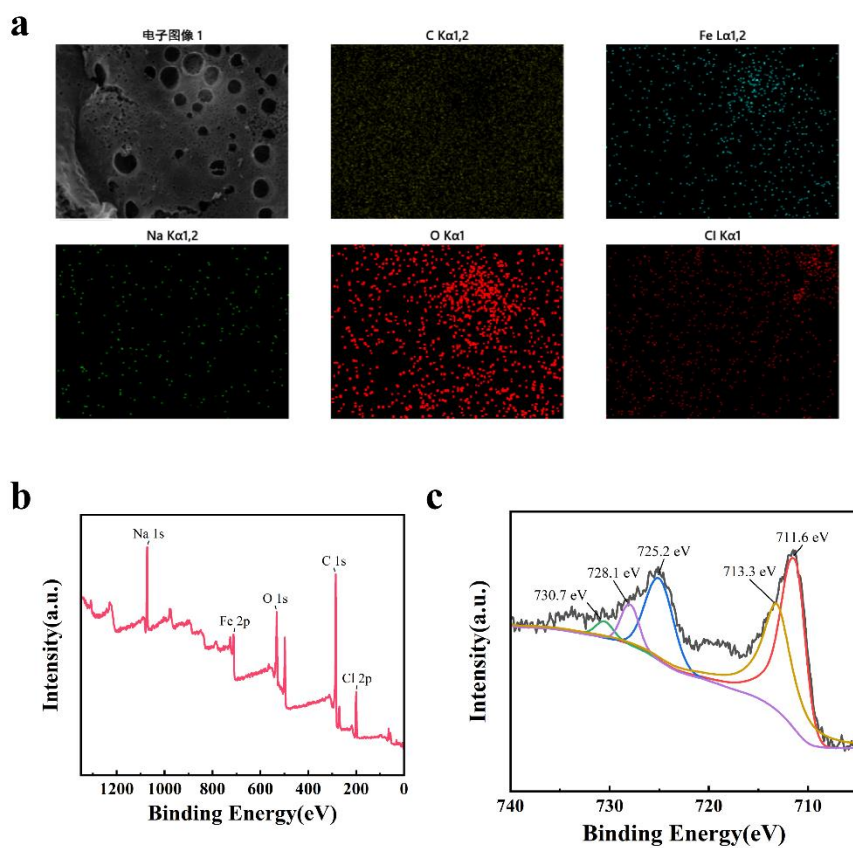
Fig. S2. EDS and XPS characterization of nanoporous carbon electrode. (a) EDS elemental distributions for cartilage-like interface structure of electrolyte-electrode interface. (b) Full XPS spectrum. (c) High-resolution Fe spectra.

As shown in Fig. S2a, EDS analyses indicate the elemental composition at the electrolyte-electrode interface (EEI) where C, Fe, Na, O, Cl could be detected. It is clear that these elements come from carbonization of $PAANa/FeCl_3$ composites. Nanoporous carbon with Fe species attached to provide pseudocapacitive under acid condition is selected as electrodes for in situ preparation of seamless interlocked EEI.
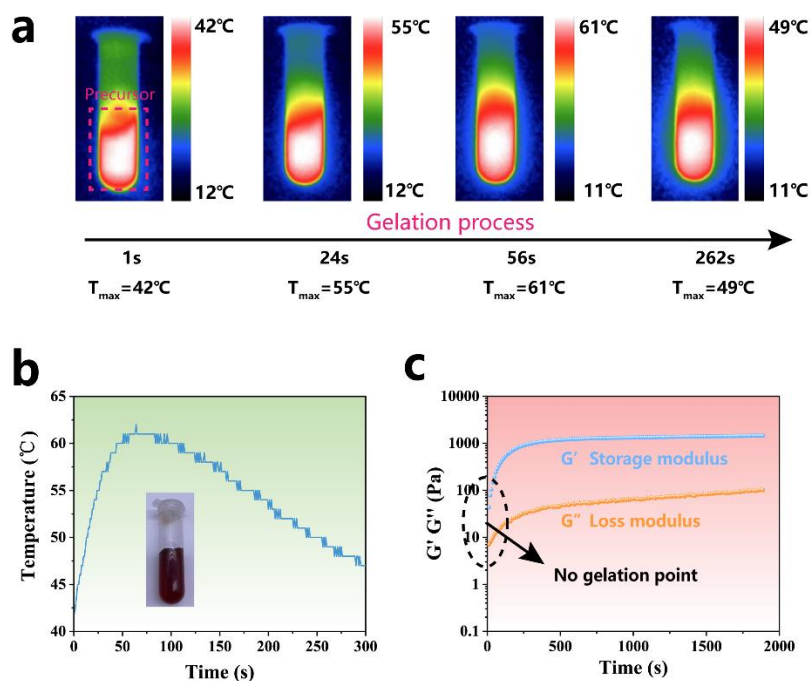
Fig. S3. Ultrafast gelation process catalyzed by Fe[Gly]$_2$ and H$_2$O$_2$ system at room temperature. a) Photographs and infrared thermal graphs captured by an optical camera and an infrared thermographic camera at different times. Temperature detected in gel system showed a sharp increase in 1s, indicating the beginning of the polymerization reaction. The maximum temperature (T$_{max}$) in the middle part of gel increased following the reaction time, reaching the peak value of 61℃ in less than one minute, which showed the ultrafast gelation process. b) Temperature variation as time during rapid gelation. The temperature-rising rate is much faster than temperature-decreasing rate, showing the rapid and continuous gelation process. c) EPR spectrum of the carbon radical and hydroxy radicals formed in H$_2$O$_2$/Fe[Gly]$_2$ initiation system. The highly efficient polymerization was further confirmed by rheological tests, where no gelation point was detected between the curve of the storage modulus (G') and that of loss modulus (G'') due to the ultrafast polymerization process.
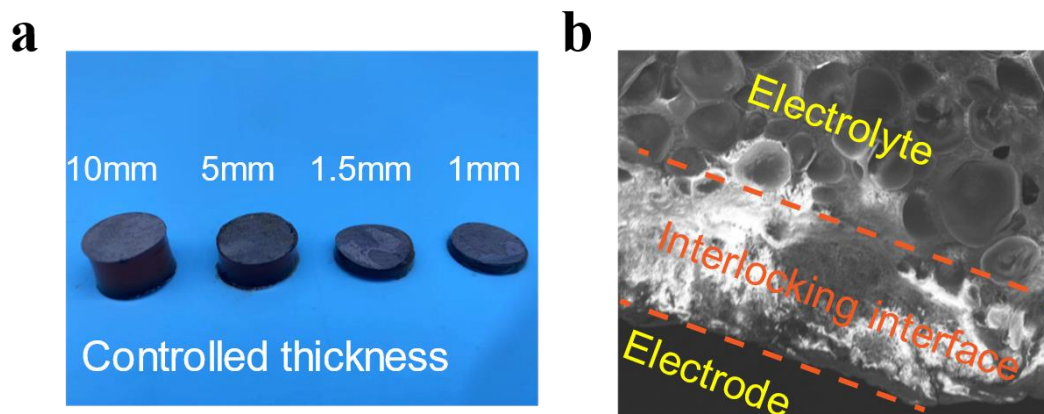
Fig. S4. Macroscopic and microscopic characterization electrode-electrolyte material. (a) The optical image of electrode-electrolyte material with controlled thickness via tuning volumes of gel precursor. (b) SEM image of MHEEI-$A_{0.15}G_{0.01}$ after swelling in water for 30min. Enlarged pore size of polymer matrix was observed, while the interlocked interface maintained the dense and entangled structure.
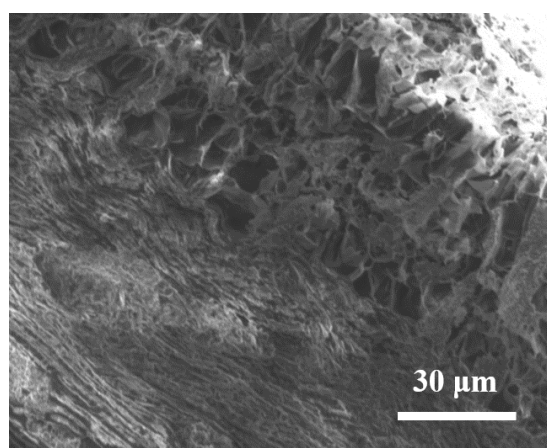
Fig. S5. SEM image of MEEI-$A_{0.15}G_{0.01}$with obvious close-cell microstructure.
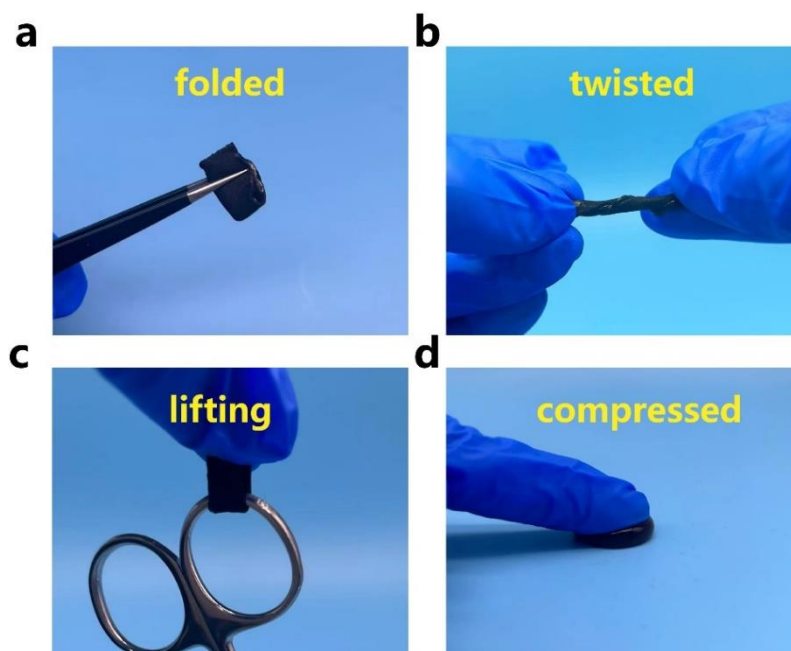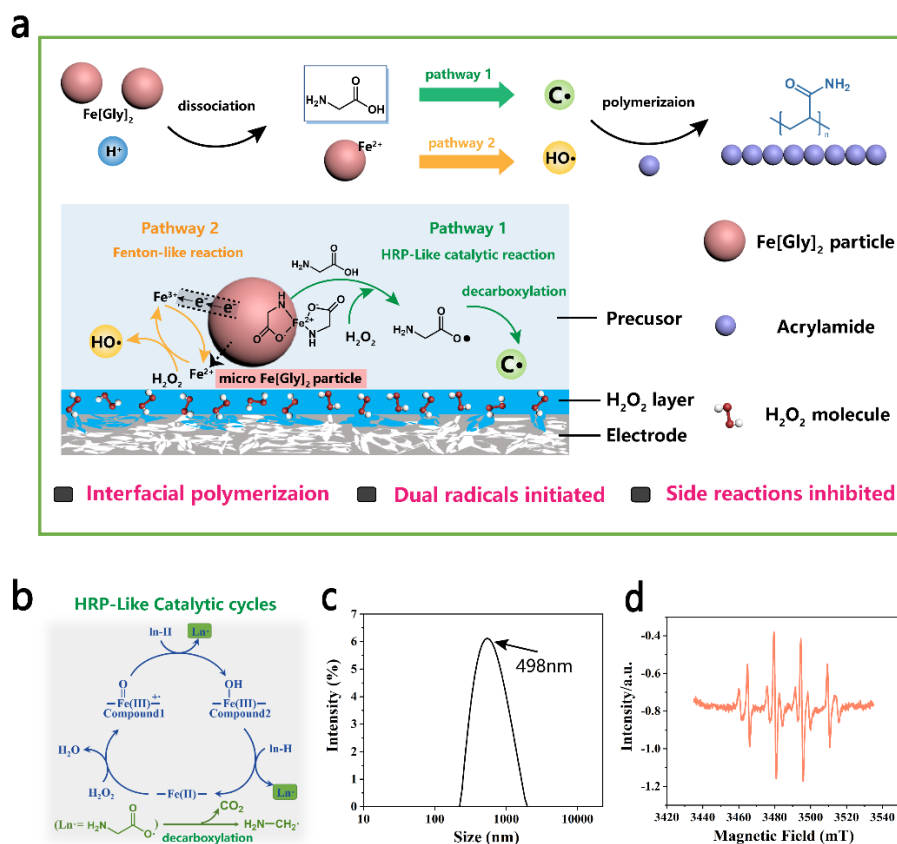
Figure S6. Optical image of mechanical deformation of in-situ gel with MHEEI.
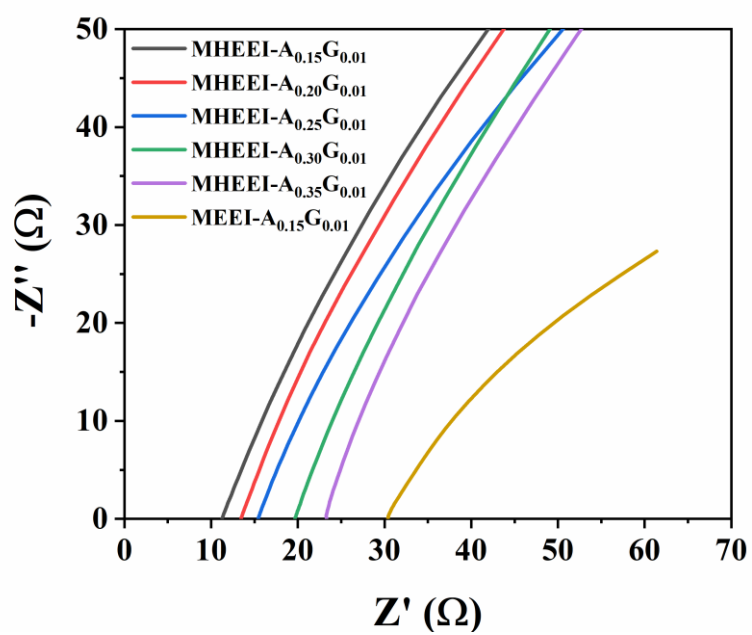
Figure S7. Frequency dependent impedance plots of MHEEI for in-situ gel with different monomer concentrations. R_b is 11.3Ω, 13.5Ω, 15.4Ω, 19.7Ω, 23.3Ω, for

MHEEI and 30.4Ω for MEEI, respectively. Ionic conductivity is calculated in Table S1.


Figure S8. (a) The reaction mechanism for rapid polymerization in $H_2O_2/Fe[Gly]_2$ initiation system. (b) Proposed catalytic mechanism for the production of Fe-based intermediate and carbon radicals. (c) Size distribution analyzed by Dynamic Light Scattering (DLS). (d) EPR spectrum of the carbon radical and hydroxy radicals formed in $H_2O_2/Fe[Gly]_2$ initiation system.

In order to investigate the highly efficient $H_2O_2/Fe[Gly]_2$ initiation system, the EPR characterization was used to examine radical species. As shown in EPR spectrum of Fig. S8d, carbon radical and hydroxyl radical peaks were detected simultaneously, in which the DMPO-C signal was observed by using DMPO as capture agent. Carbon

radicals and hydroxyl radicals generated from different pathways. Seen from the Fig. S8a, Fe[Gly]$_2$ particles were protonated to produce partial free Fe^{2+} ions and glycine molecules. Then hydroxyl radicals and carbon radicals were produced by pathway 1 and pathway 2, respectively. Regarding the production of carbon radicals, we suggested the possible mechanism of enzymatic polymerization shown in the Fig. S8b. The core of the catalytic reaction involved the interconversion of divalent and trivalent irons, forming the cycle of the electronic transfer. Firstly, divalent irons were oxidized to Fe(III)=O named Compound1, accompanied by reduction of H$_2$O$_2$ to H$_2$O. Following Fe(III)=O gained one electron from one molecule of substrate (Ln-H), the second active intermediate Fe(III)-OH named Compound2 was produced. Compound2 underwent the same catalytic process where another molecule of substrate (Ln-H) lost one electron to reduce Fe(III)-OH to Fe(II), which generated amounts of radicals (Ln·). Benefited from decarboxylation, large carbon radicals to initiate acrylamide monomers polymerization were finally produced. To verify the possible mechanism, we used H$_2$O$_2$/FeC$_2$O$_4$ and H$_2$O$_2$/Fe[Glu]$_2$ (Ferrous gluconate) initiation system containing organic ligand. As expected, acrylamide monomers were polymerized in seconds on the electrode (Fig. S19) for production of relatively stable carbon radicals. In addition, the enzymatic process was accompanied by dissociation of Fe[Gly]$_2$ to free Fe^{2+}. The free Fe^{2+} underwent another reaction route of pathway 2. Specifically, HO· was generated by Fenton-like reaction of Fe^{2+}/H$_2$O$_2$ system in which free Fe^{2+} is oxidized by H$_2$O$_2$. Fenton reaction often involves numerous side reactions and its by-products such as HO$_2$·. HO$_2$· has the ability to react with H$_2$O$_2$ to produce O$_2$ known as the polymer inhibitor to result uncontrolled polymerization process.[1-3] However, in the mimic enzyme system of ferrous glycinate (Fe[Gly]$_2$) and H$_2$O$_2$, the amounts O$_2$ produced from H$_2$O$_2$/Fe[Gly]$_2$ initiation system was, to some extent, inhibited. Benefited from Fe[Gly]$_2$ particles at the nanoscale (~500nm) showed in Fig. S8c, Fe^{3+} was adsorbed at the surface of Fe[Gly]$_2$ particle which was attached at the solid-phase of porous electrode and react slowly with liquid-phase of H$_2$O$_2$ to generate O$_2^-$·/HO$_2$·, leading to steady release of O$_2$. Moreover, electron transfer from the micro particle was beneficial to reduction of Fe^{3+} to Fe^{2+} and side reactions were inhibited. Thereby, under dual

radicals of C· and HO· initiation, ultrafast polymerization and gelation was completed. Moreover, dual radicals diffused vertically from the electrode to precursor and gradient polymer matrix was then constructed in seconds. Consequently, a seamless and tough MHEEI was successfully constricted in seconds between the in-situ gel and NC electrode.
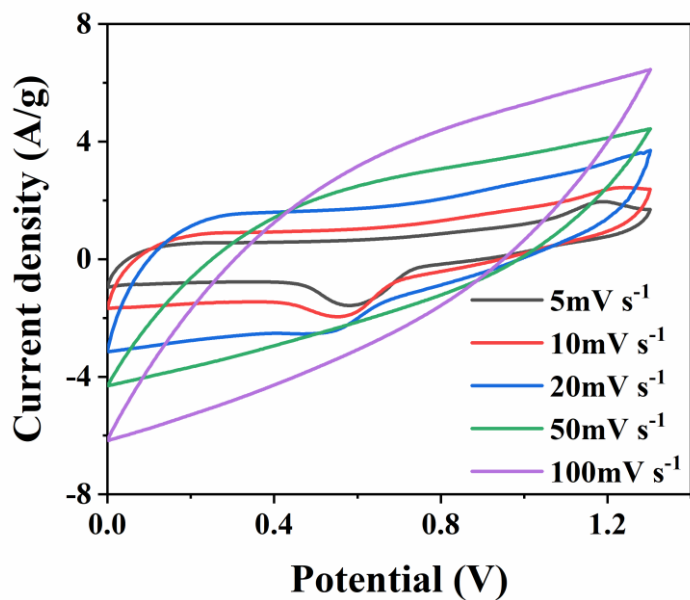

Figure S9. The cyclic voltammetry curves of MHEEI-$A_{0.15}G_{0.01}$ based supercapacitors at a scan rate from 5 mV s^{-1} to 100 mV s^{-1}.
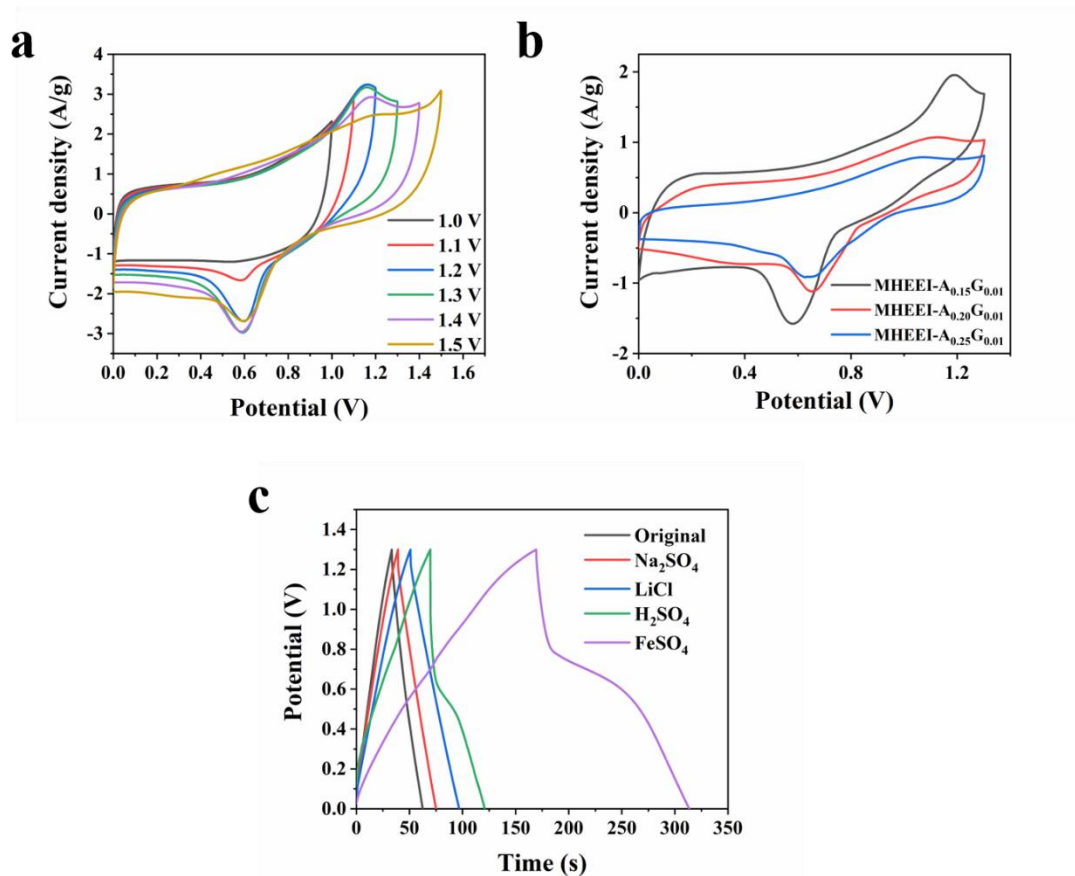
Figure S10. (a) CV curves of MHEEI-$A_{0.15}G_{0.01}$ sample tested at different potential at 20 mV/s. (b) The cyclic voltammetry curves of MHEEI based supercapacitors at a scan rate of 5 mV s^{-1}. (c) GCD curve of different gel electrolyte-based supercapacitors at a current density of 1 A/g.
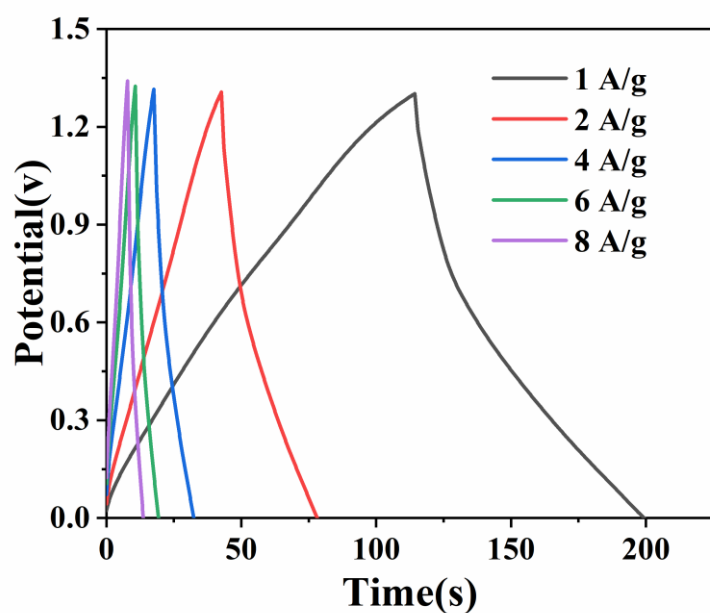
Figure S11. Galvanostatic charge-discharge curves of MEEI-$_{0.15}$G$_{0.01}$ based supercapacitor at a current density from 1A/g to 8 A/g.
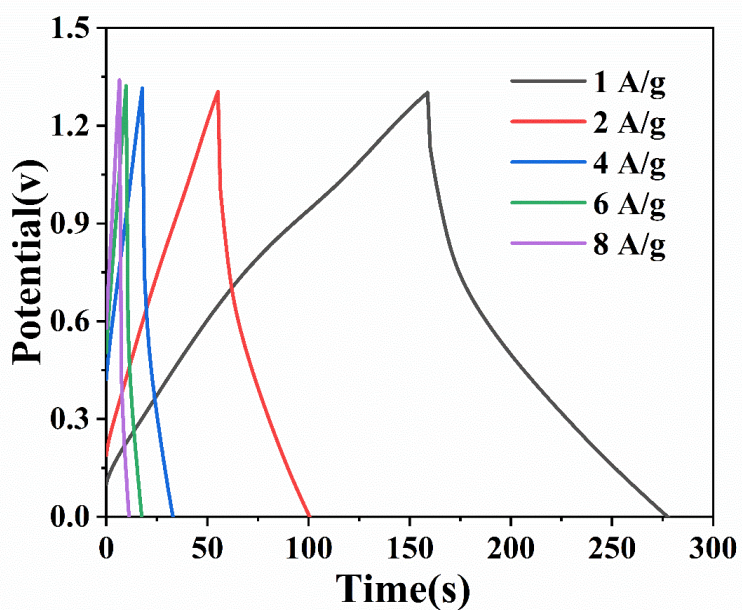
Figure S12. Galvanostatic charge-discharge curves of MHEEI-A$_{0.25}$G$_{0.01}$ based supercapacitor at a current density from 1A/g to 8 A/g.
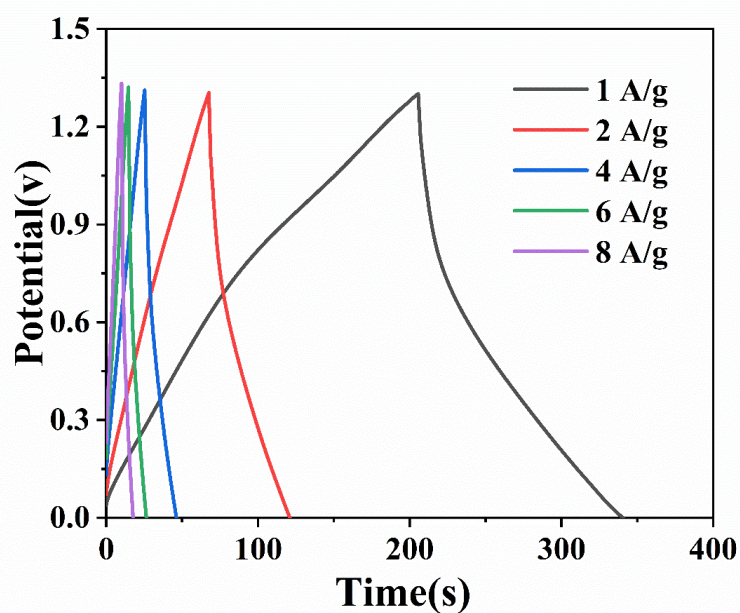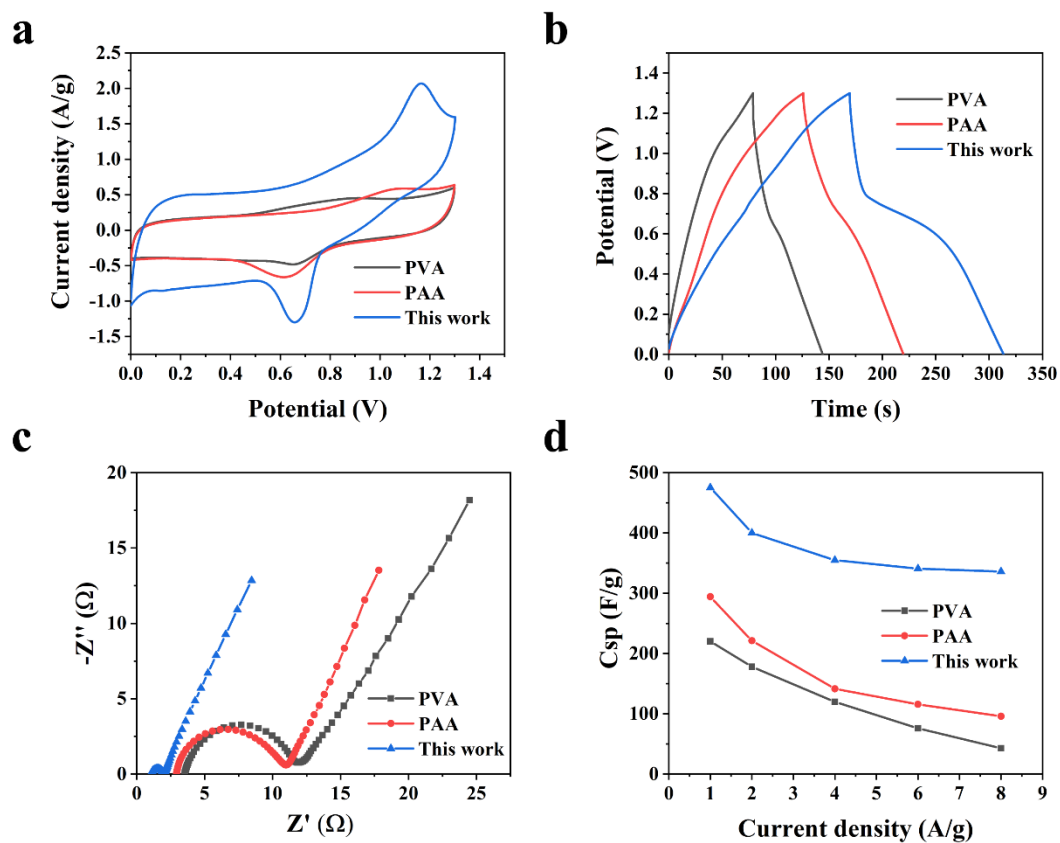
Figure S13. Galvanostatic charge-discharge curves of MHEEI-A$_{0.20}$G$_{0.01}$ based supercapacitor at a current density from 1A/g to 8 A/g.

Figure S14. The comparison of electrochemical performance between PAM/Gelatin DN gel and commonly used gel (PAA, PVA). (a) CV curve of three gel- based supercapacitors at scan rate of 5 mV/s. (b) GCD curve of three gel-based supercapacitors at a current density of 1 A/g. (c) Nyquist plots of three gel-based supercapacitors. (d) The specific capacitance of three gel-based supercapacitors at different current density.
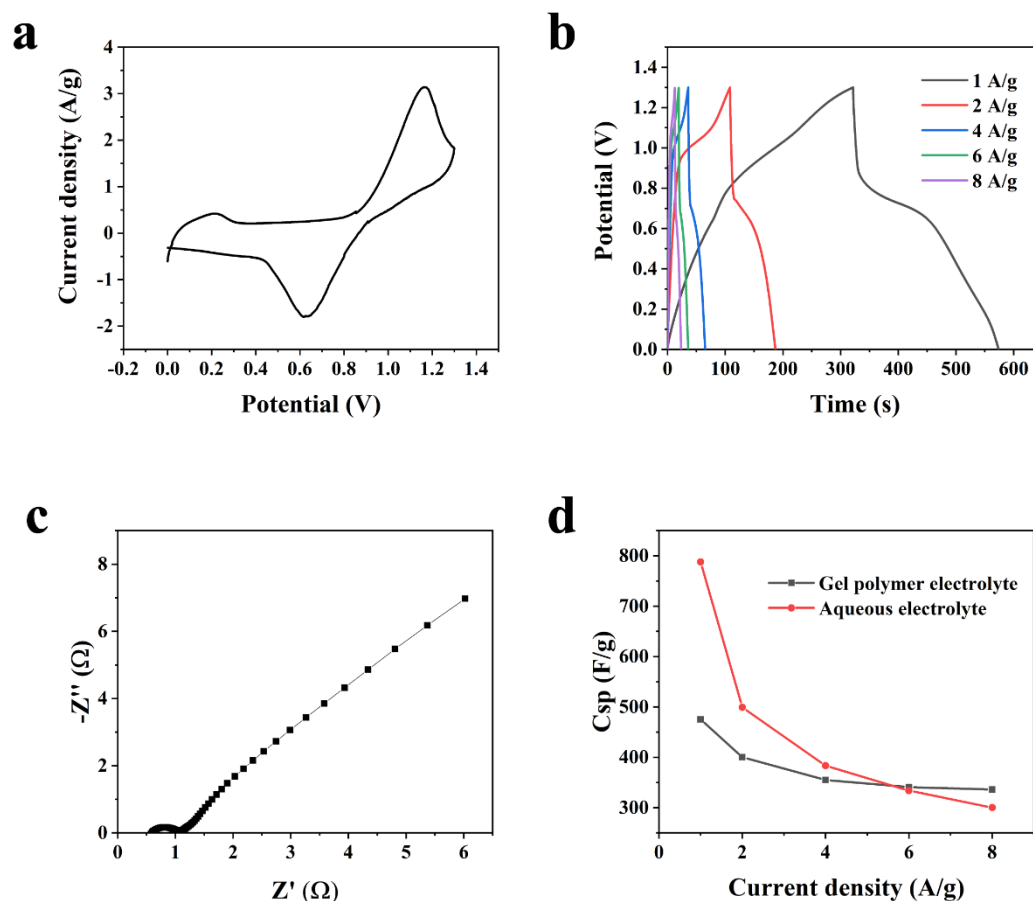
Fig. 15. performance of nanoporous carbon electrode in aqueous electrolyte. (a) CV curve of nanoporous carbon electrode in acidified 0.5M FeSO$_4$ aqueous solution. (b) GCD curves measured at different current density. (c) The Nyquist plots of aqueous electrolyte-based supercapacitor. (d) The comparison of specific capacitance of supercapacitors based on gel polymer electrolyte and aqueous electrolyte at different current density.

We evaluated the performance of nanoporous carbon electrode in aqueous electrolyte. As shown in Fig. S15a, obvious redox peaks showed around 0.6/1.1 V, implying Fe^{2+}/Fe^{3+} migrated fast at the electrode-electrolyte interface. The situation is consistent with that of gel polymer electrolyte based supercapacitors. GCD curves seen in Fig. S15b showed more obvious plateau, which was ascribed to the fact that higher ionic conductivity could achieve in aqueous electrolyte compared with gel electrolyte with polymers restricting ions migrating along the polymer chains. Accordingly, the low R_{ct} of 1.2 Ω could also be observed in Fig. S15c due to the ideal electrochemical reactions at the surface of nanoporous carbon electrode. In addition, we further compared the specific capacitance between these two typical supercapacitors. As shown in Fig. S15d, the higher C_{sp} (787.8 F/g) achieved for aqueous electrolyte based supercapacitors at 1A/g. However, as the current density increased, the gap between the C_{sp} is minimized. Especially at 8 A/g, the C_{sp} (336 F/g) for gel polymer based supercapacitors exceeded that (300 F/g) of aqueous electrolyte based. In order to compare numerically the rate performance of two supercapacitors, we calculated the capacitance retention. Gel polymer electrolyte based supercapacitors retained 70.7% retention, while aqueous electrolyte based retained 38.1%, demonstrating the merits of gel electrolytes characterized by retaining water molecules and inhibiting the splitting of water compared aqueous electrolyte.
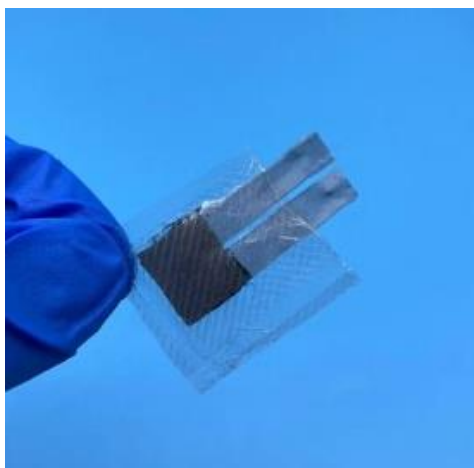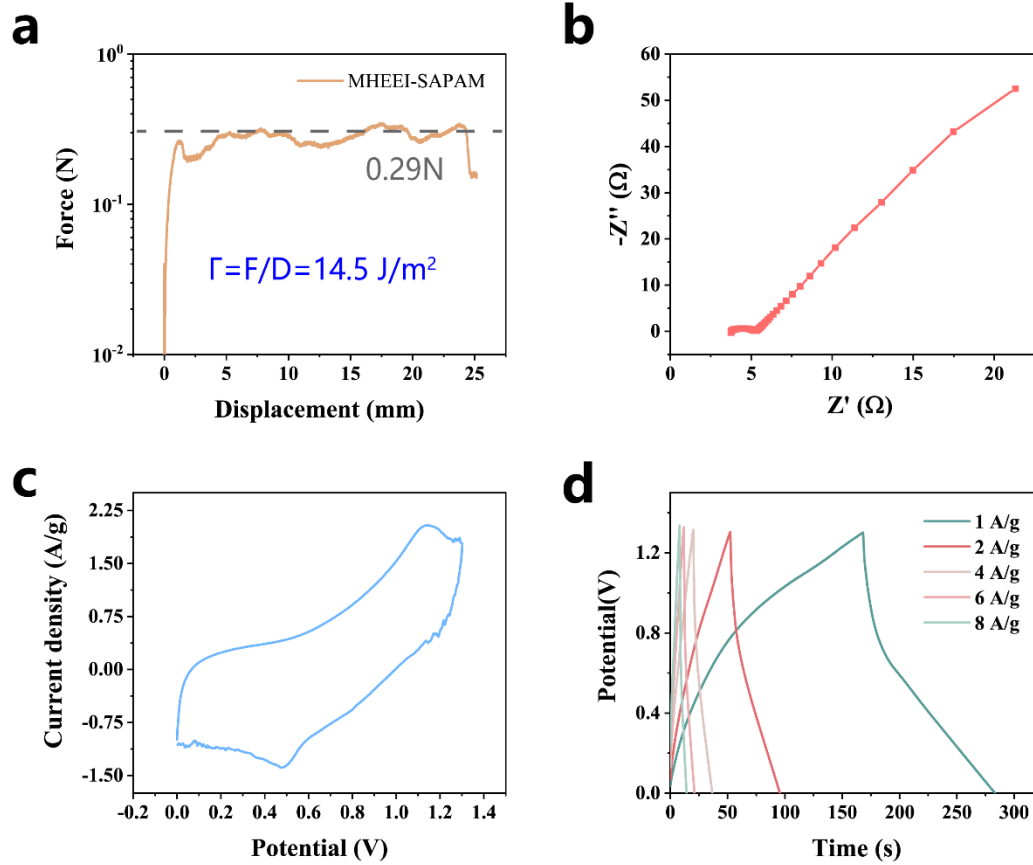
Figure S16. The optical image of the packing of the pouch cell.
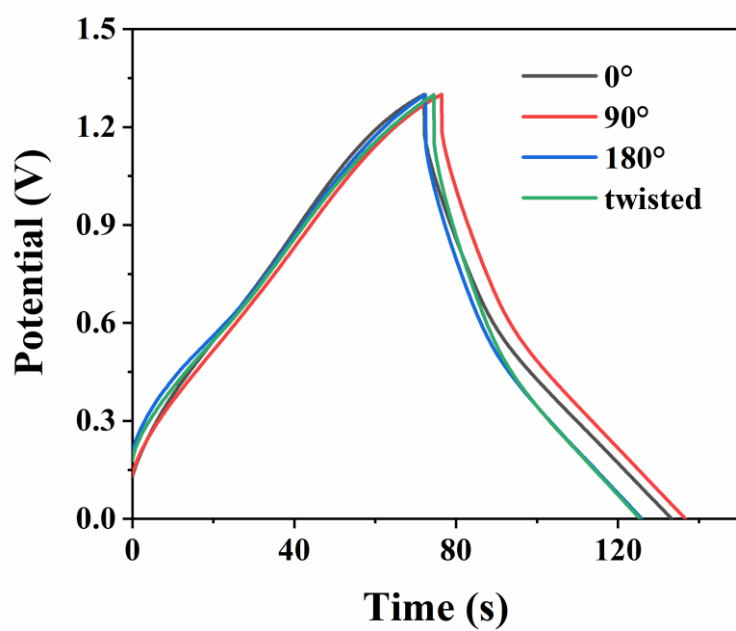
Figure S17. Galvanostatic charge-discharge curves of MHEEI-$A_{0.25}G_{0.01}$ based flexible supercapacitor at different bending angles or twisted deformation.
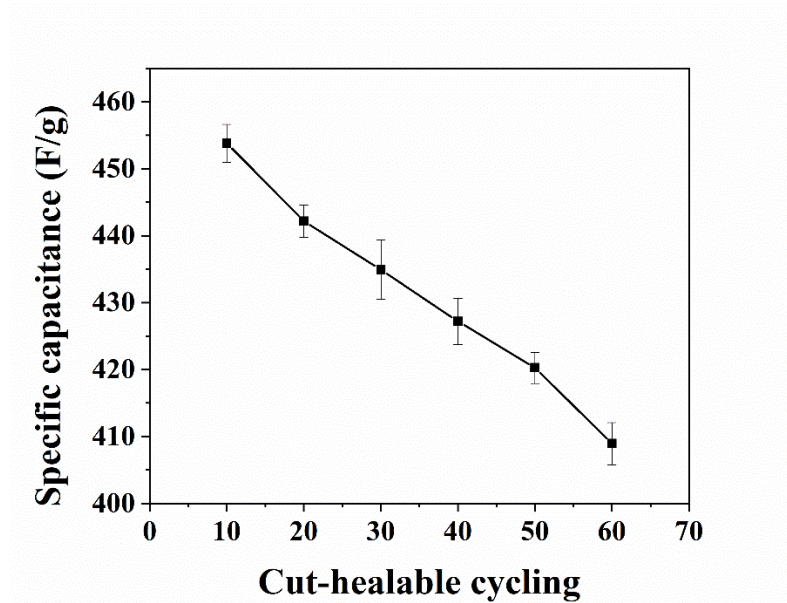
Figure S18. Healable performance of MHEEI based PAM/Gelatin DN gel at different cut-healable cycling.
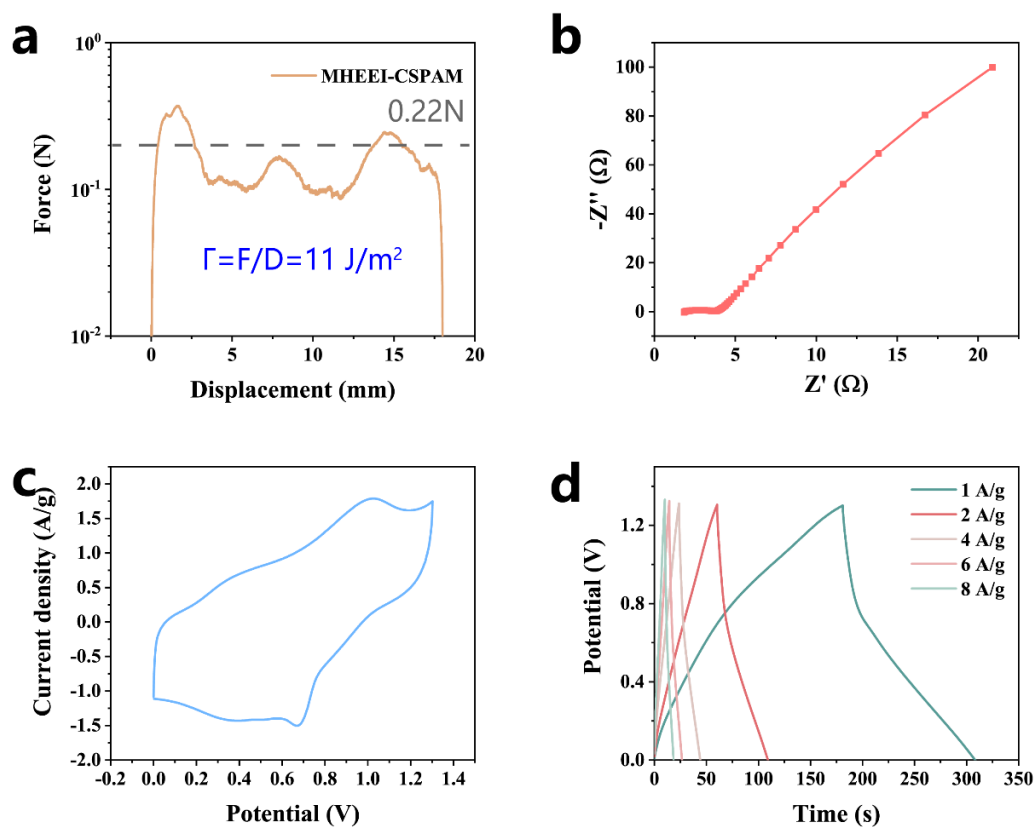
Figure S20. Mechanical and electrochemical property of MHEEI-CSPAM based on supercapacitor. a) 90-degree peel test of MHEEI-CSPAM with 11 J/m^2 interfacial toughness. b) The Nyquist plots of in situ supercapacitor based on MHEEI-CSPAM. c) CV curve with a pair of redox peaks (0.6 and 1.1V). d) GCD curve from 1A/g to 8 A/g.
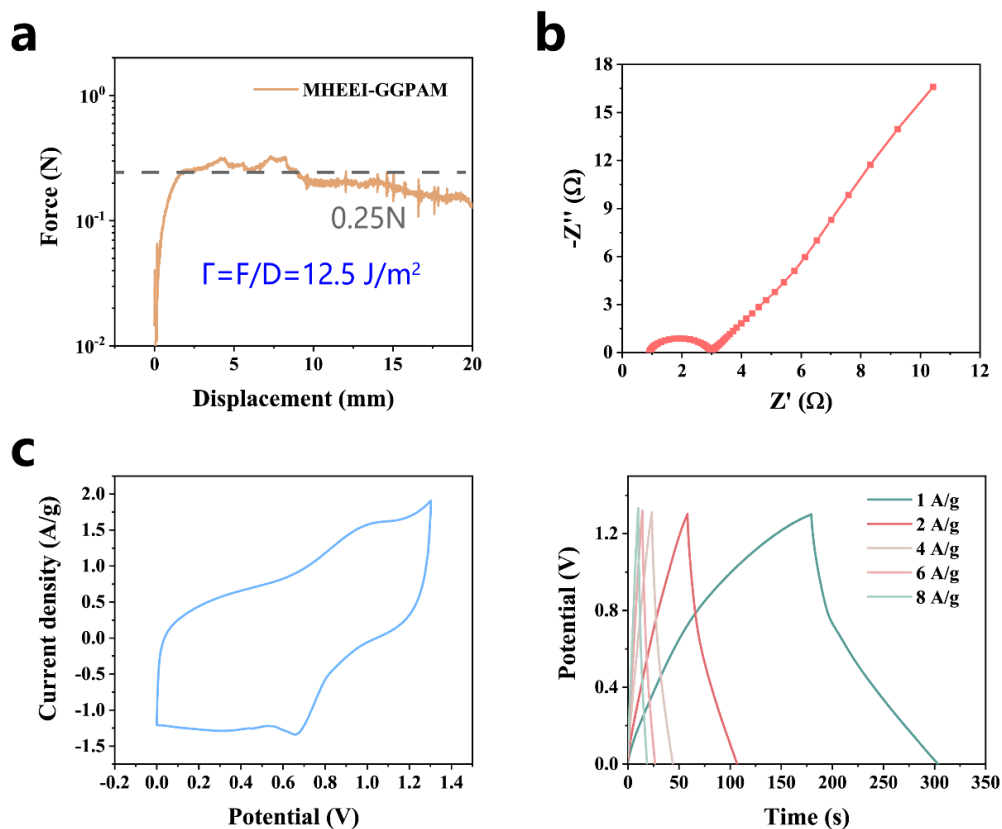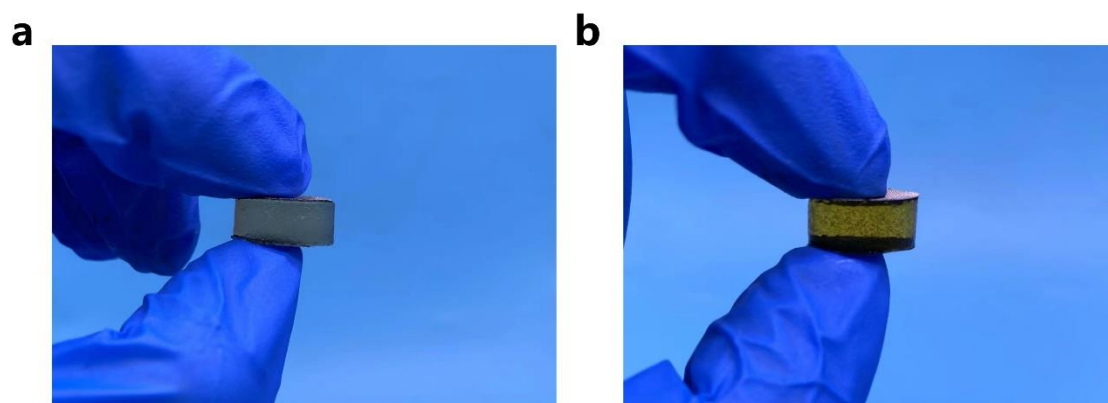
Figure S21. Mechanical and electrochemical property of MHEEI-GGPAM based supercapacitor. a) 90-degree peel test of MHEEI-GGPAM with 12.5 J/m^2 interfacial toughness. b) The Nyquist plots of in situ supercapacitor based on MHEEI-GGPAM. c) CV curve with a pair of redox peaks (0.6 and 1.1 V). d) GCD curve from 1 A/g to 8 A/g.

Figure S22. a) Sandwiched model of MHEEI based materials obtained by ultrafast gelation aided by FeC$_2$O$_4$ and H$_2$O$_2$ redox system. b) Sandwiched model of MHEEI based materials obtained by ultrafast gelation aided by Fe[Glu]$_2$ and H$_2$O$_2$ redox system.

Table S1. Ionic conductivity of in-situ/ex-situ gel with MHEEI/MEEI

Sample	Thickness L (cm)	Diameter D (cm)	Area A (cm^2)	Bulk resistance R$_b$ (Ω)	Ionic conductivity σ (S/cm)	Ionic conductivity σ (mS/cm)
MHEEI-A$_{0.15}$G$_{0.01}$	1.0	1.4	1.5386	11.3	0.0575	57.5
MHEEI-A$_{0.20}$G$_{0.01}$	1.0	1.4	1.5386	13.5	0.0481	48.1
MHEEI-A$_{0.25}$G$_{0.01}$	1.0	1.4	1.5386	15.4	0.0422	42.2
MHEEI-A$_{0.30}$G$_{0.01}$	1.0	1.4	1.5386	19.7	0.033	33.0
MHEEI-A$_{0.35}$G$_{0.01}$	1.0	1.4	1.5386	23.3	0.0279	27.9
MEEI-A$_{0.15}$G$_{0.01}$	1.0	1.4	1.5386	30.4	0.0214	21.4

Table S2. Specific capacitance, energy density and power density of MHEEI-A$_{0.15}$G$_{0.01}$

Current density I/m (A/g)	Discharge time Δt (s)	Voltage after IR drop Δv (v)	Specific capacitance C$_{sp}$ (F/g)	Energy density E (Wh/kg)	Power density P (W/kg)
1	144.1	1.26	457.5	25.2	629.8
2	56	1.12	400.0	17.4	1118.6
4	22.4	1.01	354.9	12.6	2025.0
6	12.5	0.88	340.9	9.2	2649.6
8	8.3	0.79	336.2	7.3	3166.3

Table S3. Comparison of our work with other reported flexible supercapacitors.

Electrolyte	Specific capacitance Csp (F/g)	Current density (A/g)	Capacitance retention (%)	Cycles	Ref.
PAM/Gelatin/FeSO$_4$	406	2	92.1	20000	This work
Ligtin/Gelatin/KOH	141	1	81	6000	7
Cellulose/PDA/PAM/ FeCl$_3$	172	1	84.7	10000	8
PVP/Na$_2$SO$_4$	243	1	85.8	10000	9

Alginate/MXene/CaCl$_2$	68.1	1	64	10000	10
PVA/H$_2$SO$_4$	171	1	79	5000	11
PVA/LiNO$_3$	48.8	1	83.1	5000	12
VHSNPs/PAA/H$_2$SO$_4$	215	1	80	5000	13

Notes and references

1 A. Reyhani, T.G McKenzie, Q. Fu and G. Qiao, *Macromol. Rapid Commun.*, 2019, **40**, 1900220.

2 A. Reyhani, T. G. McKenzie, H. Burachaloo, Q. Fu and G. Qiao, *Chem. Eur. J.*, 2017, **23**, 722 –7226.

3 F. S. Dainton and M. Tordoff, *Trans. Faraday Soc.*, 1957, **53**, 499-511.

4 W. H. Zuo, C. Y. Xie, P. Xu, Y. Li, J. P. Liu, *Adv. Mater.*, 2017, **29**, 1703463.

5 Q. M. Tu, L. Fan, F. Pan, J. L. Huang, Y. Gu, J. M. Lin, M. Huang, Y.Huang, J. H. Wu, *Electrochim. Acta*, 2018, **268**, 562-568.

6 N. Yadava and S. A. Hashmi, *J. Mater. Chem. A*, 2020, **8**, 18266-18279.

7 J. Wang, C. Gao, P. Hou, Y. Liu, J. Zhao, P. Huo, *Chem. Eng. J.*, 2023, **455**, 140952.

8 L. Li, F. X. Lu, C. Wang, F. L. Zhang, W. H. Liang, S. Kuga, Z. C. Dong, Y. Zhao, Y. Huanga and M. Wu, *J. Mater. Chem. A*, 2018, **6**, 24468-24478.

9 J. X. Zhang, X. Zhao, Z. Huang, T. Xu, Q. H. Zhang, *Carbon*, 2016, **107**, 844-851.

10 J. Yang, Y. Wang, J. Du, F. Bu, Q. Cao, T. Meng, X. Xu, C. Guan, *J. Mater. Chem. A*, 2022, **10**, 16409-16419.

11 N. Sheng, S. Y. Chen, J. Yao, F. Guan, M. Zhang, B. Wang, Z. Wu, P. Ji, H. P. Wang, *Chem. Eng. J.*, 2019, **368**, 1022-1032.

12 H. Jiang, X. Cai, Y. Qian, C. Zhang, L. Zhou, W. Liu, B. Li, L. Lai and W. Huang, *J. Mater. Chem. A*, 2017, **5**, 23727-23736.

13 E. Feng, W. Gao, Z. Yan, J. J. Li, Z. Li, X. Ma, L. H. Ma, Z. M. Yang, *J. Power*

Sources, 2020, **479**, 229100.

S2 Supplementary Videos

Video S1 Thermal imaging of rapid gelation process initiated by $Fe[Gly]_2$ and H_2O_2

Video S2 The rapid gelation process of in situ GPE (producing MHEEI) with controlled thickness

Video S3 LED bulb lighted with potential range of 1.8-2.0 by combining two supercapacitors

Video S4 The electric circuit repairing process aided by ultrafast construction interlocking structure at the interface